CMS Physics Analysis Summary

Contact: cms-pag-conveners-higgs@cern.ch 2018/09/26

Search for charged Higgs bosons with the $H^{\pm} \to \tau^{\pm}\nu_{\tau}$ decay channel in proton-proton collisions at $\sqrt{s} = 13$ TeV

The CMS Collaboration

Abstract

A search for charged Higgs bosons is presented in the $H^{\pm} \to \tau^{\pm}\nu_{\tau}$ decay mode in hadronic and leptonic final states. The search is based on 35.9 fb^{-1} of pp collision data recorded by the CMS experiment in 2016 at a center-of-mass energy of 13 TeV. The results agree with the expectation from the standard model. Upper limits at the 95% confidence level are set on the production cross section times branching fraction to $\tau^{\pm}\nu_{\tau}$ for a charged Higgs boson in the mass range from 80 to 3000 GeV, including the mass region near the top quark mass. The observed limit ranges from 6.0 pb at 80 GeV to 0.005 pb at 3 TeV. The limit is interpreted in the context of the MSSM m_{h}^{mod+} scenario.

1 Introduction

In 2012, the ATLAS and CMS experiments discovered a Higgs boson with a mass of 125 GeV at the CERN LHC [1–3], providing strong evidence for the spontaneous symmetry breaking via the Brout-Englert-Higgs mechanism [4–9]. The discovery was followed by precision measurements for the mass, couplings, CP quantum numbers and production rates of the new boson, which were found to be consistent with the predictions of the standard model (SM) of particle physics [10–12].

Several extensions of the SM predict a more complex Higgs sector with several Higgs fields, yielding a spectrum of Higgs bosons with different masses, charges and other properties. These models are constrained, but not excluded, by the measured properties of the 125 GeV boson. The discovery of additional Higgs boson(s) would provide unequivocal evidence for the existence of physics beyond the SM. Two-Higgs-doublet models (2HDMs) predict five different Higgs bosons: two neutral CP-even particles h and H (with $m_{\mathrm{h}} \leq m_{\mathrm{H}}$), one neutral CP-odd particle A and two charged Higgs bosons $\mathrm{H}^{\pm}$ [13]. At tree level, the 2HDM Higgs sector can be described with two parameters, conventionally chosen to be the mass of the charged Higgs boson ($m_{\mathrm{H}^{\pm}}$) and the ratio of the vacuum expectation values of the two Higgs doublets denoted as $\tan\beta$. The 2HDMs are classified into different types, depending on how the two Higgs doublets couple to fermions. This search is most sensitive to the "type-II" 2HDM, where one doublet couples to down type quarks and charged leptons, and the other to up type quarks. The minimal supersymmetric standard model (MSSM) [14] is a special case of the type-II 2HDM. Charged Higgs bosons are also predicted by more complex models, such as triplet models [15–17].

The dominant production mode of the charged Higgs boson depends on its mass. Examples of leading-order diagrams describing charged Higgs boson production in different mass regions are shown in Fig. 1. Light charged Higgs bosons, with a mass smaller than the mass difference between the top and the bottom quarks ($m_{\mathrm{H}^{\pm}} < m_{\mathrm{t}} - m_{\mathrm{b}}$), are predominantly produced in decays of top quarks (double resonant top quark production), while heavy charged Higgs bosons ($m_{\mathrm{H}^{\pm}} > m_{\mathrm{t}} - m_{\mathrm{b}}$) are produced in association with a top quark (single resonant top quark production). In the intermediate region near the mass of the top quark ($m_{\mathrm{H}^{\pm}} \sim m_{\mathrm{t}}$), the nonresonant top quark production mode also contributes and the full $\mathrm{pp} \to \mathrm{H}^{\pm}\mathrm{W}^{\mp}\mathrm{b}\bar{\mathrm{b}}$ process must be calculated in order to correctly account for all three production mechanisms and their interference [18].

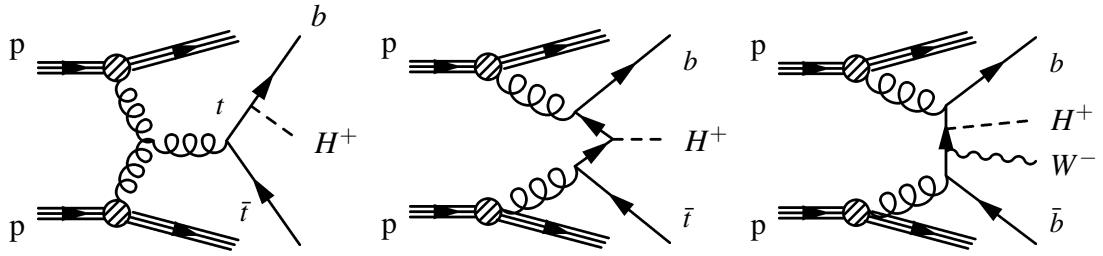

Figure 1: Leading-order diagrams describing charged Higgs boson production. Double-resonant top quark production (left) is the dominant process for light $\mathrm{H}^{\pm}$, while the single-resonant top quark production (middle) dominates for heavy $\mathrm{H}^{\pm}$ masses. For the intermediate region ($m_{\mathrm{H}^{\pm}} \sim m_{\mathrm{t}}$), both production modes and their interplay with the nonresonant top quark production (right) must be taken into account. Charge-conjugated processes are implied.

In type-II 2HDM, the light $\mathrm{H}^{\pm}$ decays almost exclusively to a tau lepton and a neutrino. For the heavy $\mathrm{H}^{\pm}$ the decay to top and bottom quarks is dominant, but as the coupling of the $\mathrm{H}^{\pm}$ to

leptons is proportional to $\tan\beta$, the branching fraction to $\tau^{\pm}\nu_{\tau}$ remains sizable for large values of $\tan\beta$.

Direct searches for charged Higgs bosons have been performed at LEP [19], at the Tevatron [20, 21], and by the LHC experiments. The ATLAS and CMS Collaborations have covered several charged Higgs boson decay channels such as $\tau^{\pm}\nu_{\tau}$ [22–28], tb [26, 29], cs [30, 31], cb [32] and $W^{\pm}Z$ [33, 34], in their previous searches at center-of-mass energies of 7, 8 or 13 TeV. Additionally, the ATLAS and CMS results on searches for additional neutral Higgs bosons have been interpreted in the 2HDM parameter space, constraining the allowed $H^{\pm}$ mass range as a function of $\tan\beta$ [35–38].

In this note a direct search for charged Higgs bosons decaying into a tau lepton and a neutrino is presented, based on data collected at a center-of-mass energy of 13 TeV by the CMS experiment in 2016, corresponding to an integrated luminosity of 35.9 fb^{-1}. The search is conducted in the fully hadronic and leptonic final states. For the hadronic final state, events contain a hadronically decaying tau lepton (τ_{h}), missing transverse momentum ($p_{\text{T}}^{\text{miss}}$) due to neutrinos and additional hadronic jets from top quark decays. The leptonic final states contain a single isolated lepton (electron or muon), $p_{\text{T}}^{\text{miss}}$ and hadronic jets. The lepton can originate either from the decays of the tau leptons from $H^{\pm}$ decays, or from a W decay.

After all selections, a transverse mass (m_{T}) distribution is reconstructed in each final state and used to search for a charged Higgs boson signal. Transverse mass is defined as

$$m_{\text{T}}(\tau_{\text{h}}/\ell) = \sqrt{2p_{\text{T}}(\tau_{\text{h}}/\ell)p_{\text{T}}^{\text{miss}}(1-\cos\Delta\phi(\vec{p}_{\text{T}}(\tau_{\text{h}}/\ell),\vec{p}_{\text{T}}^{\text{miss}}))}, \quad (1)$$

where $p_{\text{T}}(\tau_{\text{h}}/\ell)$ is the transverse momentum of the reconstructed hadronically decaying tau lepton or the isolated lepton ($\ell = \text{e}, \mu$).

Model-independent upper limits are set on the production cross section times branching fraction of the charged Higgs boson decaying into a tau lepton and a neutrino. These limits are interpreted in the context of the MSSM $m_{\text{h}}^{\text{mod+}}$ benchmark scenario [39]. A mass range from 80 GeV up to 3 TeV is covered, including the intermediate mass range near the top quark mass.

2 The CMS detector

The central feature of the CMS apparatus is a superconducting solenoid of 6 m internal diameter, providing a magnetic field of 3.8 T. Within the solenoid volume are a silicon pixel and strip tracker, a lead tungstate crystal electromagnetic calorimeter (ECAL), and a brass and scintillator hadron calorimeter, each composed of a barrel and two endcap sections. Forward calorimeters extend the pseudorapidity (η) coverage provided by the barrel and endcap detectors up to $|\eta|$=5. Muons are detected in gas-ionization chambers embedded in the steel flux-return yoke outside the solenoid. Events of interest are selected using a two-tiered trigger system [40]. The first level, composed of custom hardware processors, uses information from the calorimeters and muon detectors to select events at a rate of around 100 kHz within a time interval of less than 4 μs. The second level, known as the high-level trigger (HLT), consists of a farm of processors running a version of the full event reconstruction software optimized for fast processing, and reduces the event rate to around 1 kHz before data storage. A more detailed description of the CMS detector, together with a definition of the coordinate system used and the relevant kinematic variables, can be found in Ref. [41].

3 Event simulation

The signal samples for the light $H^{\pm}$ mass range (from 80 to 160 GeV) are generated at next-to-leading order (NLO) with the MADGRAPH5_aMC@NLO v2.3.3 [42], assuming $H^{\pm}$ production via top quark decay ($pp \to H^{\pm}W^{\mp}b\bar{b}$). For the heavy $H^{\pm}$ mass range (from 180 to 3000 GeV), the same approach is used except that $H^{\pm}$ production via $pp \to tbH^{\pm}$ is assumed. For the intermediate mass range from 165 to 175 GeV, the samples are generated at leading order (LO) using the MADGRAPH5_aMC@NLO with the model described in Ref. [18].

The effect of using LO instead of NLO samples is estimated by comparing kinematic distributions and final event yields from both types of samples in mass regions below (150–160 GeV) and above (180–200 GeV) the intermediate range. Significant differences in kinematic distributions are observed, affecting the selection efficiency and the predicted final signal yield. As the shapes of the final m_T distributions are found to have reasonable agreement, the correction is performed by scaling the final signal event yields from the intermediate samples.

The NLO/LO signal yield ratios are consistent within the 150–160 GeV and 180–200 GeV mass regions, but differ between these two regions. Thus the correction factor is calculated as an average over the NLO/LO ratios of the final event yields, separately for the 150–160 GeV and 180–200 GeV regions and separately for each final state and event category. The correction derived in the 150–160 GeV region is applied to the intermediate signal sample with $m_{H^{\pm}} = 165$ GeV, while the correction derived in the 180–200 GeV region is applied to the 170 and 175 GeV samples. For all signal samples up to $m_{H^{\pm}} = 500$ GeV, MADSPIN [43] has been used to model the decay of the $H^{\pm}$. The decays of tau leptons originating from the $H^{\pm}$ are modeled using PYTHIA 8.2 [44].

In the leptonic final states where the accurate modeling of jet multiplicity is needed for the correct categorization of events, the MG5_aMC@NLO v2.2.2 generator is used to simulate the $t\bar{t}$ events at NLO. In the hadronic final state a large amount of simulated background events is essential for the signal sensitivity and thus a larger sample generated using POWHEG v2.0 [45–49] with FxFx jet mathing and merging [50] is used to model the $t\bar{t}$ background. POWHEG v2.0 is used to model single top production via t-channel and tW production [51, 52], while the MADGRAPH5_aMC@NLO v2.2.2 generator is used for the s-channel. The value of m_t is set to 172.5 GeV for all $t\bar{t}$ and single top samples. W+jets and Z/γ^* events are generated at LO using the MADGRAPH5_aMC@NLO v2.2.2 with up to four noncollinear partons in the final state [53]. The diboson processes (WW, WZ, ZZ) are simulated using PYTHIA 8.2.

The simulated samples are normalized to the theoretical cross sections of the corresponding processes. For the $t\bar{t}$ background and the single top background in the s-channel and tW-channel, cross sections calculated at next-to-next-to-leading order precision are used [54, 55], yielding a $t\bar{t}$ cross section of $\sigma_{t\bar{t}} = 831.76$ pb. For single top production in the t-channel, W+jets, Z/γ^* and diboson processes NLO precision calculations are used [55–58].

For all simulated samples, the NNPDF3.0 parton distribution functions [59] are used, and the generators are interfaced with PYTHIA 8.2 to model the parton showering, fragmentation, and the decay of the tau leptons. The PYTHIA8 parameters affecting the description of the underlying event are set to the CUETP8M1 tune [60] for all processes except $t\bar{t}$, for which a customized CUETP8M2T4 tune [61] is used.

Generated events are processed through a simulation of the CMS detector based on the GEANT4 v9.4 software [62], and they are reconstructed following the same workflow that is used for data. The effect of additional soft inelastic pp interactions (pileup) is modeled by generating minimum bias collision events and mixing them with the simulated hard events. The effects

from multiple inelastic proton-proton collisions occurring per bunch-crossing (in-time pileup), as well as the effect of inelastic collisions happening in the preceding and subsequent bunch crossings (out-of-time pileup) are taken into account. The simulated events are weighted such that the final pileup distribution matches the one observed in data, as estimated from the instantaneous luminosity. For the data collected in 2016, an average of approximately 27 interactions per bunch crossing was measured.

4 Event reconstruction

Event reconstruction is based on the particle-flow (PF) algorithm [63] that aims to reconstruct and identify each individual particle in an event with an optimized combination of information from the various elements of the CMS detector. The output of the PF algorithm is a set of PF candidates, classified into muons, electrons, photons, and charged and neutral hadrons.

The collision vertices are reconstructed from particle tracks using the deterministic annealing algorithm [64]. The reconstructed vertex with the largest value of the physics-object p_{T}^2 sum is taken to be the primary pp interaction vertex. The physics objects in this case are the jets, clustered using the jet finding algorithm [65, 66] with the tracks assigned to the vertex as inputs, and the associated missing transverse momentum, calculated as the negative vector sum of the p_{T} of those jets. Muons, electrons, and hadronically decaying tau leptons are required to originate from the primary vertex. All other reconstructed vertices are attributed to pileup.

The electrons are reconstructed and their momentum is estimated by combining the momentum measurement by the tracker at the interaction vertex with the energy measurement in the ECAL. The energy of the corresponding ECAL cluster and the energy sum of all bremsstrahlung photons spatially compatible with originating from the electron tracks are taken into account. The momentum resolution for electrons with $p_{\mathrm{T}} \approx 45\,\mathrm{GeV}$ from $\mathrm{Z} \to \mathrm{ee}$ decays ranges from 1.7% for nonshowering electrons in the barrel region to 4.5% for showering electrons in the endcaps [67]. In addition, electrons are required to pass an identification requirement based on a multivariate discriminant that combines several variables describing the shape of the energy deposits in the ECAL, as well as the direction and quality of the associated tracks [68]. A tight working point with 88% identification efficiency for $\mathrm{t\bar{t}}$ events is used for the selection of events with an electron, while a loose working point with 95% efficiency is used to veto events with one or several electrons, depending on the final state.

Muons are identified as a track in the central tracker consistent with either a track or several hits in the muon system, associated with an energy deficit in the calorimeters [69]. The momenta of muons are obtained from the curvatures of the corresponding tracks. Contributions from other particles misidentified as muons are suppressed with a discriminant based on the track fit quality. As in the case of electrons, two working points are defined: a tight working point to select events with an isolated muon, and a loose one for muon veto.

The background contributions from nonprompt and misidentified leptons are suppressed by requiring the leptons to be isolated from hadronic activity in the event. For this purpose, an isolation variable is defined as the sum of the transverse momenta of PF candidates in a cone around the lepton, divided by the transverse momentum of the lepton. For optimal performance across the lepton momentum range, the cone size is varied with the lepton p_{T} as $\Delta R = \sqrt{(\Delta\eta)^2 + (\Delta\phi)^2} = 10\,\mathrm{GeV}/\min(\max(p_{\mathrm{T}}(\ell), 50\,\mathrm{GeV}), 200\,\mathrm{GeV})$, leading to cone radii from 0.05 to 0.2.

For each event, hadronic jets are clustered from the reconstructed PF candidates using the in-

frared and collinear safe anti-k_T algorithm [65, 66] with a distance parameter of 0.4. The jet momentum is determined as the vectorial sum of all particle momenta in the jet, and is found from simulation to be within 5 to 10% of the true momentum over the whole p_T spectrum and detector acceptance. Pileup can contribute additional tracks and calorimetric energy deposits to the jet momentum. To mitigate this effect, tracks identified as originating from pileup vertices are discarded and an offset correction is applied to correct for remaining contributions. Jet energy corrections are derived from simulation to bring the measured response of jets to that of particle level jets on average. In situ measurements of the momentum balance in dijet, photon + jet, Z + jet, and multijet events are used to account for any residual differences in jet energy scale between data and simulation [70]. The jet energy resolution amounts typically to 15% at 10 GeV, 8% at 100 GeV, and 4% at 1 TeV [71]. Additional selection criteria are applied to each jet to remove jets potentially dominated by anomalous contributions from various subdetector components or reconstruction failures.

Jets originating from the hadronization of b quarks (b jets) are identified using the combined secondary vertex algorithm [72, 73], combining information on the decay vertices of long-lived mesons and the impact parameters of charged particle tracks into a likelihood discriminant. The working point is chosen such that the probability to misidentify jets originating from light-flavor quarks or gluons as b jets is 1%, corresponding to 65% efficiency for the selection of genuine b jets. Simulated samples are corrected for differences in b-jet identification and misidentification efficiency compared to the data.

Hadronically decaying tau leptons are reconstructed using the hadron-plus-strips algorithm, using clustered anti-k_T jets as seeds [74, 75]. The hadron-plus-strips algorithm reconstructs different τ decay modes with one charged pion and up to two neutral pions (one-prong), or three charged pions (three-prong). As neutral pions decay promptly to a photon pair, they are reconstructed by defining strips of ECAL energy deposits in the (η, ϕ) plane. The τ_h candidates that are found to be consistent with the hypothesis of being muons or electrons misidentified as tau leptons are rejected. The jets originating from the hadronization of quarks and gluons misidentified as τ_h are suppressed using a multivariate discriminant that combines τ_h isolation and lifetime information [74].

The missing transverse momentum is defined as the negative vector sum of the p_T of all reconstructed PF candidates [76].

5 Event selection

The search is conducted in three exclusive final states, characterized by different signal sensitivities and background compositions:

- τ_h + jets: fully hadronic final state (events with isolated leptons are vetoed),
- ℓ + τ_h: leptonic final state with a hadronically decaying tau lepton (events with additional leptons are vetoed),
- ℓ + no τ_h: leptonic final state without a hadronically decaying tau lepton (events with τ_h or additional leptons are vetoed).

In the low-$m_{H^\pm}$ region, below the top quark mass, the sensitivity of the hadronic final state is limited by the relatively high trigger thresholds, making the leptonic final states most sensitive for the $H^\pm$ signal. In the high-$m_{H^\pm}$ region, above m_t, the hadronic final state dominates the sensitivity as the selection efficiency is higher and the majority of the tau leptons decay hadronically.

The event selection and categorization strategies are chosen separately for each final state to efficiently discriminate against the background events while ensuring a sufficient signal selection efficiency.

5.1 Fully hadronic final state (τ_h + jets)

An HLT trigger algorithm requiring the presence of a hadronically decaying tau lepton and missing transverse momentum is used to select the events for offline analysis. The trigger requires the tau lepton to be loosely isolated with $p_T > 50\,\text{GeV}$ and $|\eta| < 2.1$, and with a leading track transverse momentum $p_T^{\text{track}} > 30\,\text{GeV}$. The missing transverse momentum estimated based on calorimeter information is required to be larger than 90 GeV. The trigger efficiencies for the τ_h and p_T^{miss} requirements are measured separately and found to vary between 50–100% for the τ_h part of the trigger and between 10–100% for the p_T^{miss} part of the trigger, as a function of τ_h p_T and η.

The efficiency of the τ_h part of the trigger is determined with the tag-and-probe technique, using $Z/\gamma^* \to \tau^+\tau^-$ events with one hadronic and one muonic tau decay. The efficiency of the p_T^{miss} part of the trigger is evaluated from events with a signal-like topology selected with a single-τ trigger. The simulated events are corrected to match the efficiencies measured in the data.

In the offline selection, selection criteria identical to the those in the HLT are applied for the reconstructed τ_h candidate and for the missing transverse momentum that is recalculated after jet energy corrections. The one-prong τ_h candidates, corresponding to τ decays into a charged pion and up to two neutral pions, are selected for further analysis. Events are required to contain at least three jets with $p_T > 30\,\text{GeV}$ and $|\eta| < 4.7$, separated from the reconstructed τ_h by $\Delta R > 0.5$. At least one of the jets is required to pass the b-jet identification with $|\eta| < 2.4$. Any event with isolated electrons (muons) with $p_T > 15\,\text{GeV}$ ($p_T > 10\,\text{GeV}$), $|\eta| < 2.5$, and passing the loose isolation requirement is rejected.

In order to suppress the background from quantum chromodynamics (QCD) multijet events with a jet misidentified as τ_h, an additional selection on the $(\Delta\phi(\tau_h, p_T^{\text{miss}}), \Delta\phi(\text{jet}_n, p_T^{\text{miss}}))$ plane is applied. The index n runs over the three highest-p_T jets (jet_n) in the event. The QCD multijet events passing the previous selection steps typically contain a hadronic jet misidentified as the τ_h, another hadronic jet recoiling in the opposite direction, and $\vec{p}_T^{\text{miss}}$ arising from the mismeasurement of the jet momenta. They can be suppressed with a discriminant defined as

$$R_{\text{bb}}^{\text{min}} = \min_n \left\{ \sqrt{\left(180^\circ - \Delta\phi(\tau_h, \vec{p}_T^{\text{miss}})\right)^2 + \left(\Delta\phi(\text{jet}_n, \vec{p}_T^{\text{miss}})\right)^2} \right\}. \quad (2)$$

The selected events are required to have $R_{\text{bb}}^{\text{min}} > 40^\circ$. The distribution of the $R_{\text{bb}}^{\text{min}}$ variable after all other selections is shown in Fig. 2 (left).

The selected events are classified into two categories based on the value of the variable $R_\tau = p_T^{\text{track}}/p_T^{\tau_h}$, reflecting the helicity correlations emerging from the opposite polarization states of the tau leptons originating from W and $H^\pm$ decays [77]. The distribution of the R_τ variable after all other selections is shown in Fig. 2 (right). After all other selections, most of the signal events have a large value of R_τ, and the high-R_τ category provides a good signal-to-background ratio. For large $m_{H^\pm}$ values, the signal events are more evenly distributed between the two categories, so inclusion of the background-dominated low-R_τ category in the statistical analysis further improves the sensitivity for the heavy $H^\pm$. Separating the two categories at $R_\tau = 0.75$ maximizes the signal sensitivity across the $m_{H^\pm}$ range.

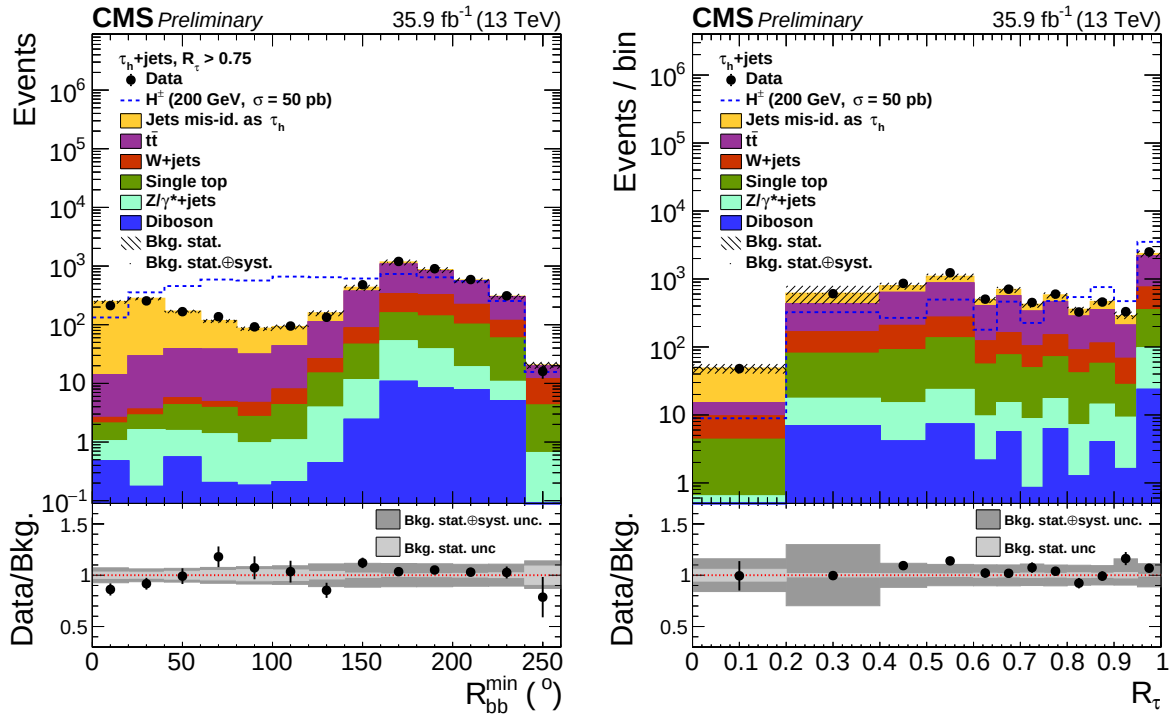

Figure 2: The distribution of the angular discriminant R_{bb}^{min} after all other selections, including $R_\tau > 0.75$ requirement, have been applied (left) and the distribution of the R_τ variable used for categorization after all other selections, including $R_{bb}^{min} > 40^\circ$ requirement, have been applied (right).

5.2 Leptonic final state with a hadronically decaying tau lepton (ℓ + τ_h)

Single lepton trigger algorithms are used for the online selection of events with isolated muons or electrons. Several HLT algorithms for muon and electron selection with different thresholds are used in *or* combination to recover efficiency at high lepton p_T values. In the offline selection, muons are required to have $p_T > 30\,\text{GeV}$ and $|\eta| < 2.4$ whereas electrons are required to have $p_T > 35\,\text{GeV}$ and $|\eta| < 2.1$ because of trigger constraints. Both electrons and muons are required to pass the tight isolation selection. Events with any additional electrons (muons) with $p_T > 10\,\text{GeV}$, $|\eta| < 2.1$ ($|\eta| < 2.4$), and passing loose identification criteria are vetoed. Efficiencies for online and offline identification of leptons are measured and the simulated events are corrected to match the efficiencies observed in data. A hadronically decaying tau lepton is required, with $p_T > 20\,\text{GeV}$, $|\eta| < 2.3$, and with a ΔR separation of at least 0.5 with respect to the lepton.

One, two or three jets are required with $p_T > 30\,\text{GeV}$ and $|\eta| < 2.4$, separated from the lepton and the τ_h by $\Delta R > 0.5$. At least one of the jets is required to pass the b-jet identification. To suppress the background from jets misidentified as tau leptons, the missing transverse momentum is required to be at least 70 GeV. The background contribution from events with muons originating from b-hadron decays is suppressed by requiring the azimuthal angle between the lepton and the missing transverse momentum ($\Delta\phi(\ell, p_T^{miss})$) to have a value greater than 0.5.

The selected events are classified into several categories for the statistical analysis. The background-enriched categories allow a precise determination of the background yields with the fit to data and extrapolation of this information to signal regions. Three categories are defined based on jet multiplicity and the number of jets passing the b-jet identification: 1j1b (one jet, also identified as a b jet), ≥2j1b and ≥2j+≥2b. A second categorization is performed in bins

of p_T^{miss}: $70 < p_T^{miss} < 100\,GeV$, $100 < p_T^{miss} < 150\,GeV$ and $p_T^{miss} > 150\,GeV$. Together with the separate electron and muon final states, this results in 18 categories. The signal-to-background ratio in different categories varies with $H^{\pm}$ mass, as jet categories with two jets and high p_T^{miss} become more sensitive for higher $m_{H^{\pm}}$. The categorization is found to improve the expected sensitivity significantly, especially in the low-$m_{H^{\pm}}$ region where efficient discrimination against backgrounds is essential.

5.3 Leptonic final state without a hadronically decaying tau lepton (ℓ + no τ_h)

The event selection criteria for the ℓ + no τ_h final state are nearly identical to those described in Section 5.2 for the ℓ + τ_h final state, except that events with any hadronic taus present are vetoed.

Two or three jets are required, each jet separated from the lepton by $\Delta R > 0.5$. Higher jet multiplicities are not selected, because they are expected to be more sensitive in searches for other charged Higgs boson decay modes, e.g. $H^{\pm} \to tb$. At least one of the jets is required to pass the b-jet identification. Jets misidentified as leptons originating from the QCD multijet events are suppressed to a negligible level by requiring a high missing transverse momentum of at least 100 GeV and by applying the following angular selections:

- $\Delta\phi(\ell, p_T^{miss}) > 0.5$,
- $\Delta\phi(\text{leading jet}, p_T^{miss}) > 0.5$,
- $\min(\Delta\phi(\ell, \text{jet}_n)) < \pi - 0.5$,

where jet_n refers to any of the selected jets in the events. The first criterion is identical to the one applied in the ℓ + τ_h final state against muons from b-hadron decays while the second discriminates efficiently against the QCD multijet background. The last requirement is designed to reject background events where all the jets are back-to-back with respect to the selected lepton.

To further enhance signal sensitivity and to constrain the backgrounds, a similar categorization as in the ℓ + τ_h final state is established. Four categories are used based on jet multiplicity and the number of jets passing the b-jet identification: 2jets+1b, 2jets+2b, 3jets+1b and 3jets+$\geq$2b, followed by two categories in p_T^{miss}: $100 < p_T^{miss} < 150\,GeV$ and $p_T^{miss} > 150\,GeV$. Together with the separate electron and muon final states, this results in 16 categories.

6 Background estimations

The dominant background processes in the hadronic final state are QCD multijet and $t\bar{t}$ production. Other backgrounds are single top production, W boson production in association with jets, Z/γ^* processes, and diboson production. We refer to $t\bar{t}$ and single top events as top events, and to W+jets, Z/γ^* and diboson events as electroweak events. The backgrounds from events containing either a genuine tau lepton or an electron or muon misidentified as τ_h are estimated from simulation, while the background from jets misidentified as tau leptons is estimated from data. The correct identification or misidentification of tau leptons is determined in the event selection by requiring a generator-level tau lepton to match with the reconstructed τ_h within a ΔR cone of 0.1.

In the leptonic final states, the dominant background is $t\bar{t}$ production in which the semileptonic $t\bar{t}$ decays are dominant in the ℓ + no τ_h final state and the dilepton $t\bar{t}$ decays dominant in the ℓ + τ_h final state. Minor backgrounds include single top production, W+jets, Z/γ^* and diboson production. QCD multijet background is suppressed to a negligible level with tight angular

selections and p_T^{miss} requirements. All backgrounds in these two final states are estimated from simulation.

6.1 Measurement of background from jets misidentified as τ_h

QCD multijet production is the dominant process in the events where a jet is misidentified as a hadronically decaying tau lepton (denoted as jet $\rightarrow \tau_h$). Even though the probability of misidentifying a jet as a tau lepton is small, the large cross section of the multijet production makes this background contribution sizable. The jet $\rightarrow \tau_h$ background is estimated using a control sample enriched in misidentified taus, obtained by inverting the offline tau isolation requirement used for signal selection. The contamination of the control region from electroweak/top events with a genuine tau or a lepton misidentified as τ_h is estimated from the simulation and subtracted from the control sample. The difference in selection efficiency between signal and control regions is accounted for by normalizing the control sample with *fake factors*, calculated at an early stage of event selection where a possible signal does not stand out from the large background yield. In order to account for the correlation between τ_h p_T and p_T^{miss} as well as geometrical differences in detector response, the measurement is performed in bins of τ_h p_T and $|\eta|$.

The background consists of two components: the QCD multijet events and electroweak/top events with jets misidentified as τ_h. The jets in these two background components have different quark and gluon composition, implying different tau fake rates. Thus the fake factors for misidentified taus from the QCD multijet events and for misidentified taus from electroweak/top events are estimated separately. The fake factor for the QCD multijet events is defined as the ratio of the two QCD multijet yields. The QCD multijet event yield in the control region is estimated by subtracting the simulated electroweak/top contribution from data. To estimate the contribution of the QCD multijet events in the signal region, a binned maximum likelihood fit of p_T^{miss} templates to data is performed, using the fraction of the QCD multijet events as a fit parameter. The p_T^{miss} shape of the QCD multijet events is assumed to be similar in signal and control regions, so that the shape observed in the control region is used as the fit template. The template for electroweak/top events is obtained directly from simulation. The fake factor for electroweak/top events is also estimated from simulation as the ratio of event yields in signal and control regions. Finally, the overall normalization of the control sample (as a function of τ_h p_T and $|\eta|$) is determined as a weighted sum of the two fake factors, where the weight corresponds to the relative fractions of the QCD multijet and electroweak/top backgrounds in the control region after all selections.

7 Systematic uncertainties

All relevant experimental and theoretical sources of uncertainty are taken into account. A summary of uncertainties considered in the anaysis given in Table 1. Some of them only affect the final event yield for a given signal or background process, while others also modify the shape of the final transverse mass distributions.

The simulated events are corrected to match the efficiencies measured in the data. For the trigger used in the τ_h + jets final state, the corresponding uncertainty is taken into account as a shape uncertainty. In the ℓ + τ_h and ℓ + no τ_h final states, the online selection with single lepton triggers is incorporated in the overall lepton identification efficiency and the corresponding normalization uncertainty.

The systematic uncertainties on identification and isolation efficiencies for tau leptons, elec-

Table 1: Effect of systematic uncertainties on the final event yields in %, prior to the fit, summed over all final states and categories.

Source	Shape	$H^{\pm}$	Jets $\to \tau_h$	$t\bar{t}$	Single top	Electroweak
$\tau_h + p_T^{miss}$ trigger efficiency	✓	1.4	2.0	0.2	0.2	0.2
τ_h identification	✓	1.8	0.6	1.1	1.0	0.9
Lepton selection efficiency		2.3	—	2.7	2.7	2.7
Jet energy scale and resolution	✓	4.7	0.4	5.1	9.2	13.4
τ_h energy scale	✓	0.2	0.6	< 0.1	< 0.1	< 0.1
Unclustered p_T^{miss} energy scale	✓	2.6	< 0.1	3.2	5.2	7.2
b-jet identification	✓	3.6	0.8	3.1	3.4	13.8
Luminosity		2.5	0.4	2.5	2.5	2.5
Pileup	✓	1.1	< 0.1	0.8	1.2	4.0
Jets mis-id. as τ_h estimation	✓	—	6.1	—	—	—
Cross section (RF scales, PDF)		—	0.8	5.5	5.3	3.6
Top quark mass		—	0.4	2.7	2.2	—
Acceptance (RF scales, PDF)		5.1	0.5	2.8	2.8	6.8
$t\bar{t}$ parton showering		—	—	6.1	—	—

trons, and muons are taken into account. All the measured efficiencies are found to be compatible with the simulated ones within the uncertainties. The agreement of the tau identification efficiency between data and simulated samples is measured using the tag-and-probe technique [75]. The uncertainty in the measurement is 5%. It is taken into account as a normalization uncertainty and anti-correlated between the ℓ + no τ_h final state and the final states with a τ_h. For tau leptons with large transverse momentum, an additional uncertainty of $^{+5}_{-35}\% p_T$ / TeV is applied in the hadronic final state as a shape uncertainty, in order to cover for possible differences arising in the extrapolation of the measured efficiencies to the high-p_T range. Simulated events with an electron or muon misidentified as a hadronically decaying tau lepton are weighted to obtain the misidentification rates measured in data. The correction is applied as a function of η and the corresponding shape uncertainty is taken into account.

For the selection of electrons (muons), the combined uncertainty in online selection and offline identification is 3% (4%). For leptons vetoed with loose identification and isolation criteria the effect of this uncertainty in the final event yield is typically only 0.3%. Both effects are taken into account as normalization uncertainties.

The systematic uncertainties related to the calibration of energy measurement for jets, τ_h and p_T^{miss} are considered as shape uncertainties. The uncertainties in the jet energy scale and jet energy resolution are taken into account as a function of jet p_T and η. The uncertainty due to the τ_h energy scale is $\pm 1.2\%$ for τ_h $p_T < 400\,\text{GeV}$ and $\pm 3\%$ otherwise [75]. The variations of jet and tau energy scales are propagated to $\vec{p}_T^{miss}$, for which uncertainties arising from the unclustered energy deposits in the detector are also taken into account. The uncertainty in the lepton energy scale is found to be negligible for this analysis. Correcting the b-jet identification and misidentification efficiencies in simulated samples affects the final m_T shapes, so the related uncertainties are considered as shape uncertainties [73].

The systematic uncertainty due to the pileup modeling is obtained by shifting the mean of the total inelastic pp production cross section by $\pm 5\%$ around its nominal value [78], and propagating the difference to the final m_T distributions as a shape uncertainty. The uncertainty in the measurement of the integrated luminosity is 2.5% [79].

Uncertainties related to the jet $\to \tau_h$ background measurement in the fully hadronic final state are included. The statistical uncertainties in the data and simulated samples used to determine the fake factors are propagated into the final m_T distributions as a normalization uncertainty. A possible difference in the shapes of m_T distributions in the signal and control regions is incorporated as a shape uncertainty. Both contributions affect the final jet $\to \tau_h$ event yield by approximately 5%. As the jet $\to \tau_h$ background is estimated by subtracting simulated events (electroweak/top contribution) from the control data sample, all uncertainties related to the simulated samples are propagated to this background.

The reference cross sections used to normalize each simulated background process are varied within their theoretical uncertainties related to the choice of renormalization and factorization (RF) scales and the parton distribution functions. For $t\bar{t}$ and single top processes, the effect of the top quark mass on the cross sections is considered by varying m_t by 1.0 GeV around the nominal value of 172.5 GeV. Theoretical uncertainties in the acceptance of signal and background events are determined by varying the RF scales and parton distribution functions [80] and are applied as normalization uncertainties.

The uncertainty arising from the parton shower modeling is included for the dominant $t\bar{t}$ background in the leptonic final states. Four variations are considered perturbing the initial and final state parameters [81], the matching of the matrix element to the parton shower, and the underlying event tune [61]. The parton shower uncertainties are derived in each category and are applied as normalization uncertainties, uncorrelated between categories.

The statistical uncertainties related to the finite amount of events in the final m_T distributions are taken into account using the Barlow–Beeston method [82].

8 Results

A simultaneous binned maximum likelihood fit is performed over all the categories in the three final states. In total 36 m_T distributions are fitted. The templates are binned according to the precision of the samples, leading to wider bins in the tail of the distributions. The systematic uncertainties are incorporated as nuisance parameters in the likelihood. They are profiled in the fit according to their probability density functions, taking correlations into account. For normalization uncertainties, log-normal probability density functions are used as priors. For shape uncertainties, polynominal interpolation is used to derive continuous prior distributions from the nominal and varied m_T shape templates. The expected event yields after a background-only fit to the data and the observed yields are summarized in Table 2. The distributions of m_T after a background-only fit to the data are shown in Fig. 3 for both categories in the τ_h + jets final state, in Fig. 4 for the two categories with high signal sensitivity in the ℓ + τ_h final state, and in Fig. 5 for two high-sensitivity categories in the ℓ + τ_h final state, in the ℓ + no τ_h final state. No significant excess is observed in any of the categories, and the result of the simultaneous fit is found to agree with the standard model prediction.

The modified frequentist CL_s criterion [83, 84] based on the profile likelihood ratio test statistic [85] is applied to determine the 95% confidence level (CL) limit for the $H^\pm$ production cross section $\sigma_{H^\pm}$ times the branching fraction $\mathcal{B}(H^\pm \to \tau^\pm \nu_\tau)$. The asymptotic approximation [86] is used throughout the analysis.

For the $H^\pm$ mass range up to 165 GeV, the limit on $\mathcal{B}(t \to bH^\pm)\mathcal{B}(H^\pm \to \tau^\pm \nu_\tau)$ is calculated, scaling down the $t\bar{t}$ background component consistently with the $\mathcal{B}(t \to bH^\pm)$ signal hypothesis, and the result is interpreted as a limit on $\sigma_{H^\pm}\mathcal{B}(H^\pm \to \tau^\pm \nu_\tau)$ by assuming

Table 2: Number of expected and observed events for the three final states after all selections, summed over all categories in each final state. For background processes, the event yields after background-only fit and the corresponding uncertainties are shown. For the $H^{\pm}$ mass hypotheses of 100, 200 and 2000 GeV, the signal yields are normalized to the $H^{\pm}$ production cross section of 1 pb and the total systematic uncertainties (prior to the fit) are shown.

Process	τ_h + jets	ℓ + τ_h	ℓ + no τ_h
$H^{\pm}$ signal, $m_H^{\pm} = 100$ GeV	20 ± 3	160 ± 20	241 ± 26
$H^{\pm}$ signal, $m_H^{\pm} = 200$ GeV	156 ± 22	327 ± 37	682 ± 61
$H^{\pm}$ signal, $m_H^{\pm} = 2000$ GeV	1627 ± 310	369 ± 24	1571 ± 99
Jets mis-id. as τ_h	4619 ± 35	—	—
$t\bar{t}$	1455 ± 13	30556 ± 466	174744 ± 346
Single top	801 ± 13	3006 ± 49	26128 ± 261
Electroweak	1739 ± 18	2760 ± 37	52314 ± 223
Total expected from the SM	8614 ± 42	36322 ± 500	253187 ± 398
Observed	8647	36277	253236

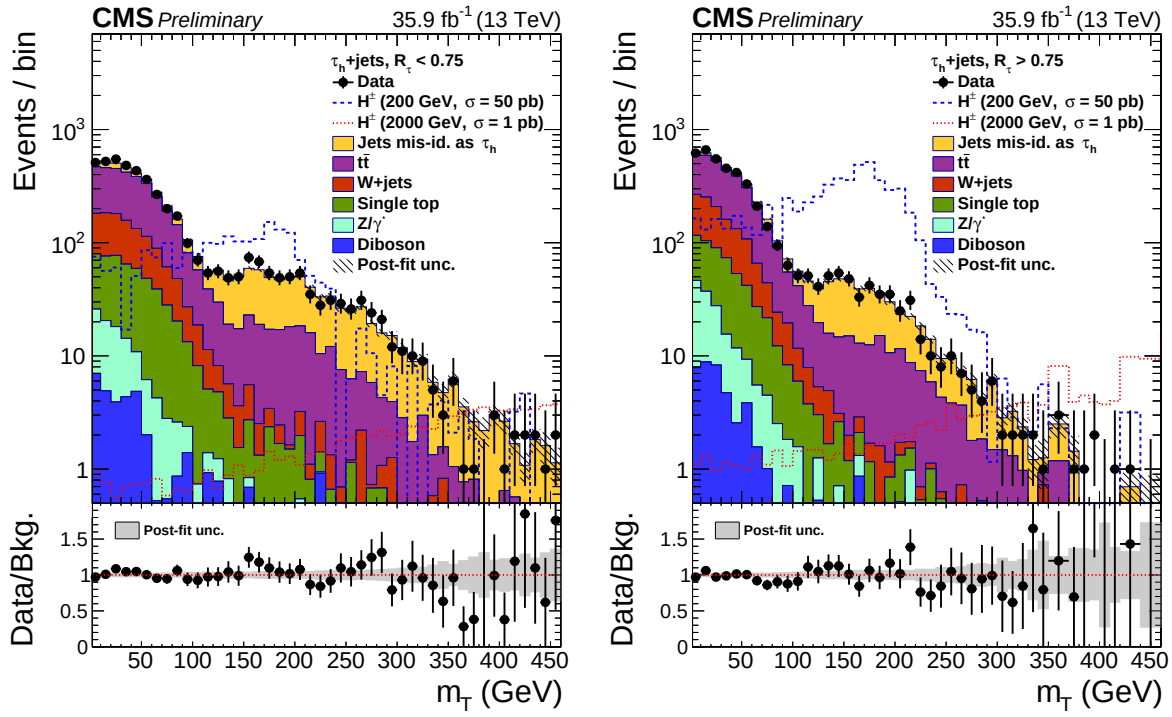

Figure 3: The transverse mass distributions in the fully hadronic final state after a background-only fit to the data, for the categories defined by $R_\tau < 0.75$ (left) and $R_\tau > 0.75$ (right).

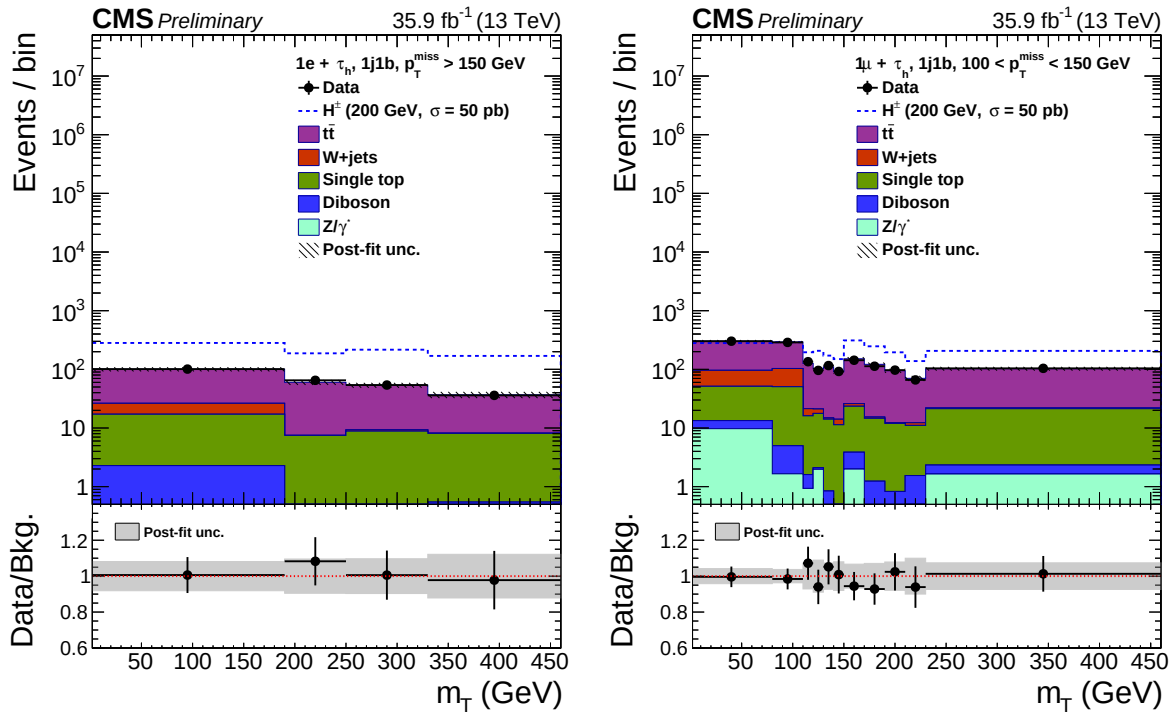

Figure 4: The transverse mass distributions for two $\ell + \tau_h$ categories with high signal sensitivity after a background-only fit to the data. Left: category with one electron, one τ_h, one jet identified as a b jet and $p_T^{miss} > 150\,GeV$. Right: category with one muon, one τ_h, one jet identified as a b jet and $100 < p_T^{miss} < 150\,GeV$.

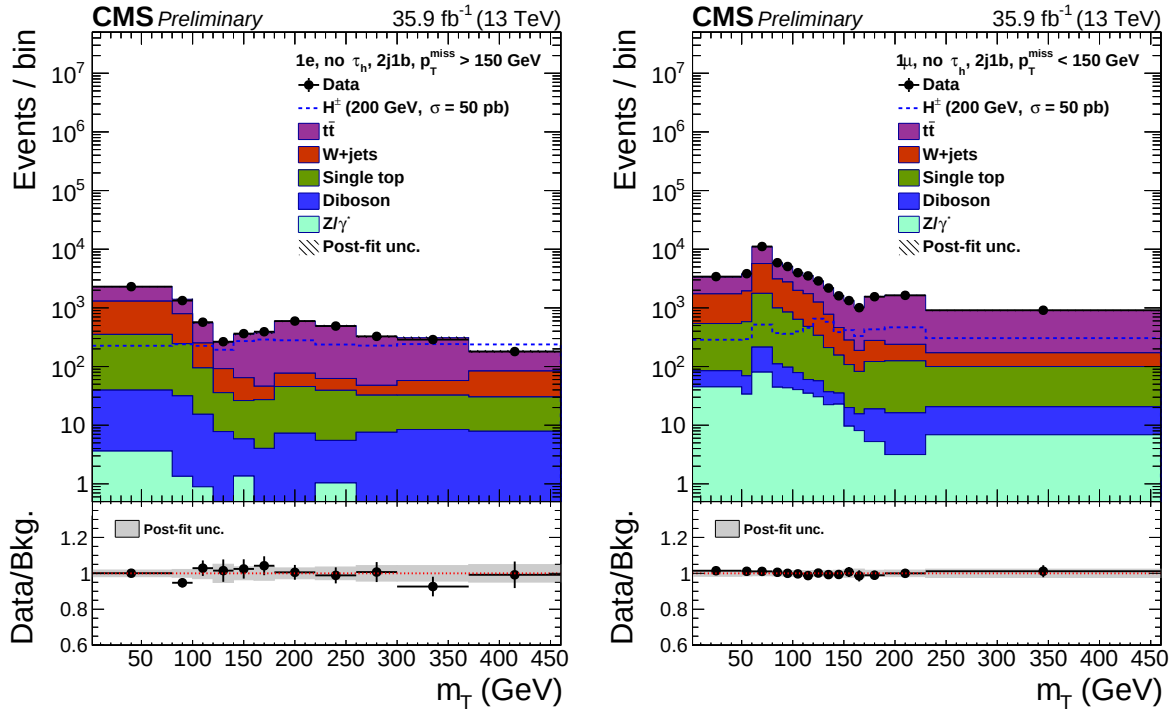

Figure 5: The transverse mass distributions for ℓ + no τ_h categories with high signal sensitivity after a background-only fit to the data. Left: category with one electron, no identified τ_h, two jets (one of them identified as a b jet) and $p_T^{miss} > 150\,GeV$. Right: category with one muon, no identified τ_h, two jets (one of them identified as a b jet) and $p_T^{miss} < 150\,GeV$.

$\sigma_{H^\pm} = 2\sigma_{t\bar{t}}\mathcal{B}(t \to bH^\pm)(1 - \mathcal{B}(t \to bH^\pm))$. For the $H^\pm$ mass range from 170 GeV to 3 TeV, the limit on $\sigma_{H^\pm}\mathcal{B}(H^\pm \to \tau^\pm\nu_\tau)$ is calculated without assuming a specific production mode.

The model-independent upper limit with all final states and categories combined is shown on the left side of Fig. 6. The numerical values are listed in Table 3. The observed limit ranges from 6.0 pb at 80 GeV to 0.005 pb at 3 TeV. For the light charged Higgs mass range of 80–160 GeV, the limit corresponds to $\mathcal{B}(t \to bH^\pm)\mathcal{B}(H^\pm \to \tau^\pm\nu_\tau)$ values between 0.36% (at 80 GeV) and 0.08% (at 160 GeV).

This limit is interpreted in the MSSM m_h^{mod+} benchmark scenario by comparing the observed limit on the $H^\pm$ cross section to the theoretical cross sections predicted in this scenario [18, 87–91]. The limit for the MSSM m_h^{mod+} scenario on the $(m_{H^\pm}, \tan\beta)$ plane is shown on the right side of Fig. 6. All $\tan\beta$ values are excluded for m_h values up to 150 GeV.

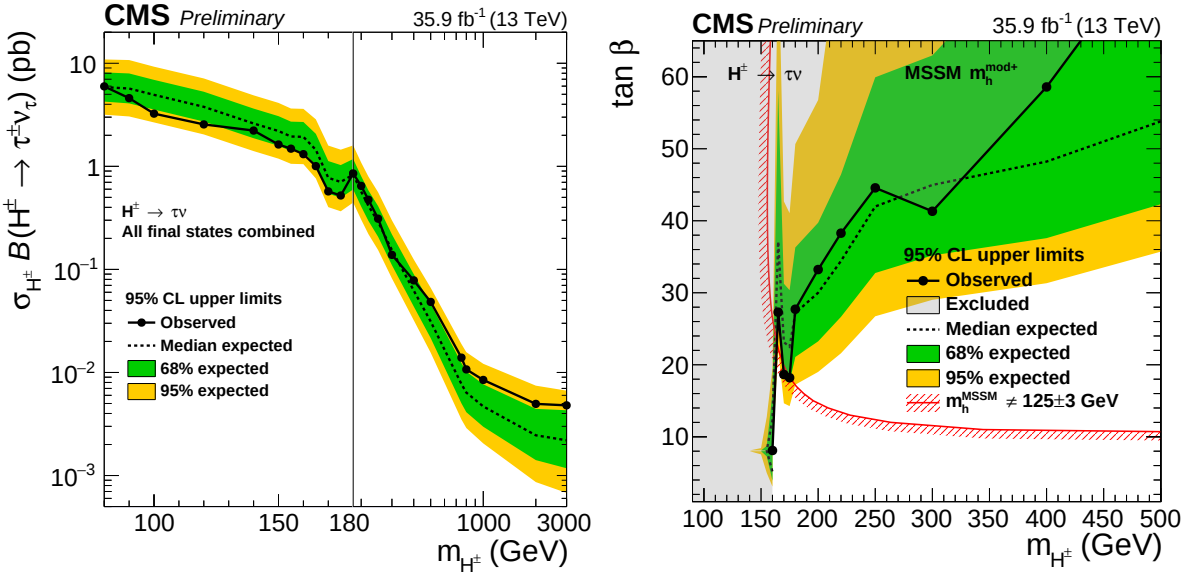

Figure 6: The observed 95 % CL exclusion limits on $\sigma_{H^\pm}\mathcal{B}(H^\pm \to \tau^\pm\nu_\tau)$ (solid black points), compared to the expected limit assuming only standard model processes (dashed line) for the $H^\pm$ mass range from 80 to 3000 GeV (left), and the same limit interpreted in m_h^{mod+} benchmark scenario (right). The green (yellow) error bands represent one (two) standard deviations from the expected limit. On the left, the horizontal axis is linear from 80 to 180 GeV and logarithmic for larger $m_{H^\pm}$ values. On the right, the region below the red line is excluded assuming that the observed neutral Higgs boson is the light CP-even 2HDM Higgs boson with a mass of 125 ± 3 GeV, where the uncertainty is the theoretical uncertainty in the mass calculation.

9 Summary

A search for charged Higgs bosons decaying as $H^\pm \to \tau^\pm\nu_\tau$ has been presented, using events recorded by the CMS experiment in 2016 at a center-of-mass energy of 13 TeV. Transverse mass distributions are reconstructed in hadronic and leptonic final states, and are found to agree with the standard model expectation. Upper limits for the $H^\pm$ production cross section times the branching fraction are set at 95% confidence level for a $H^\pm$ mass ranging from 80 GeV to 3 TeV, including the mass range close to the top quark mass. The observed limit ranges from 6.0 pb at 80 GeV to 0.005 pb at 3 TeV. The results are interpreted as constraints in the parameter space of the MSSM m_h^{mod+} benchmark scenario. In this scenario, all $\tan\beta$ values are excluded for charged Higgs boson masses up to 150 GeV.

Table 3: The expected and observed 95% CL exclusion limits on $\sigma_{H^\pm}\mathcal{B}(H^\pm \to \tau^\pm\nu_\tau)$ for the $H^\pm$ mass range from 80 to 3000 GeV. The ± 1 s.d. (± 2 s.d.) refers to one (two) standard deviations from the expected limit.

$m_{H^\pm}$	Expected limit (pb)					Observed
(GeV)	-2 s.d.	-1 s.d.	median	+1 s.d.	+2 s.d.	limit (pb)
80	3.17	4.25	5.87	8.15	10.89	5.97
90	3.05	4.08	5.69	7.96	10.75	4.59
100	2.67	3.56	4.94	6.90	9.26	3.24
120	2.04	2.72	3.78	5.29	7.12	2.55
140	1.41	1.87	2.61	3.63	4.88	2.22
150	1.19	1.58	2.20	3.07	4.14	1.63
155	1.06	1.41	1.95	2.71	3.64	1.48
160	1.05	1.39	1.93	2.69	3.61	1.31
165	0.76	1.02	1.45	2.67	2.86	1.01
170	0.40	0.54	0.77	1.12	1.59	0.57
175	0.37	0.50	0.71	1.03	1.45	0.52
180	0.44	0.60	0.83	1.18	1.59	0.85
200	0.30	0.41	0.57	0.80	1.9	0.65
220	0.22	0.30	0.41	0.58	0.80	0.47
250	0.15	0.21	0.29	0.41	0.56	0.31
300	0.08	0.11	0.15	0.22	0.30	0.14
400	0.032	0.043	0.062	0.090	0.125	0.078
500	0.016	0.022	0.031	0.046	0.067	0.048
750	0.0035	0.0050	0.0077	0.012	0.019	0.014
800	0.0029	0.0041	0.0064	0.0102	0.0157	0.0107
1000	0.0020	0.0030	0.0047	0.0077	0.0121	0.0085
2000	0.0009	0.0014	0.0025	0.0044	0.0074	0.0050
2500	0.0007	0.0012	0.0022	0.0042	0.0068	0.0047
3000	0.0007	0.0012	0.0022	0.0043	0.0067	0.0048

References

[1] ATLAS Collaboration, "Observation of a new particle in the search for the standard model Higgs boson with the ATLAS detector at the LHC", *Phys. Lett. B* **716** (2012) 1, doi:10.1016/j.physletb.2012.08.020, arXiv:1207.7214.

[2] CMS Collaboration, "Observation of a new boson at a mass of 125 GeV with the CMS experiment at the LHC", *Phys. Lett. B* **716** (2012) 30, doi:10.1016/j.physletb.2012.08.021, arXiv:1207.7235.

[3] CMS Collaboration, "Observation of a new boson with mass near 125 GeV in pp collisions at $\sqrt{s}$ = 7 and 8 TeV", *JHEP* **06** (2013) 081, doi:10.1007/JHEP06(2013)081, arXiv:1303.4571.

[4] P. W. Higgs, "Broken symmetries, massless particles and gauge fields", *Phys. Lett.* **12** (1964) 132, doi:10.1016/0031-9163(64)91136-9.

[5] P. W. Higgs, "Broken Symmetries and the Masses of Gauge Bosons", *Phys. Rev. Lett.* **13** (1964) 508, doi:10.1103/PhysRevLett.13.508.

[6] G. S. Guralnik, C. R. Hagen, and T. W. B. Kibble, "Global Conservation Laws and Massless Particles", *Phys. Rev. Lett.* **13** (1964) 585, doi:10.1103/PhysRevLett.13.585.

[7] P. W. Higgs, "Spontaneous Symmetry Breakdown without Massless Bosons", *Phys. Rev.* **145** (1966) 1156, doi:10.1103/PhysRev.145.1156.

[8] T. W. B. Kibble, "Symmetry breaking in non-Abelian gauge theories", *Phys. Rev.* **155** (1967) 1554, doi:10.1103/PhysRev.155.1554.

[9] F. Englert and R. Brout, "Broken Symmetry and the Mass of Gauge Vector Mesons", *Phys. Rev. Lett.* **13** (1964) 321, doi:10.1103/PhysRevLett.13.321.

[10] ATLAS and CMS Collaborations, "Measurements of the Higgs boson production and decay rates and constraints on its couplings from a combined ATLAS and CMS analysis of the LHC pp collision data at $\sqrt{s} = 7$ and 8 TeV", *JHEP* **08** (2016) 045, doi:10.1007/JHEP08(2016)045, arXiv:1606.02266.

[11] ATLAS Collaboration, "Study of the spin and parity of the Higgs boson in diboson decays with the ATLAS detector", *Eur. Phys. J. C* **75** (2015) 476, doi:10.1140/epjc/s10052-015-3685-1, arXiv:1506.05669. [Erratum: doi:10.1140/epjc/s10052-016-3934-y].

[12] CMS Collaboration, "Constraints on the spin-parity and anomalous HVV couplings of the Higgs boson in proton collisions at 7 and 8 TeV", *Phys. Rev. D* **92** (2015) 012004, doi:10.1103/PhysRevD.92.012004, arXiv:1411.3441.

[13] G. C. Branco et al., "Theory and phenomenology of two-Higgs-doublet models", *Phys. Rept.* **516** (2012) 1, doi:10.1016/j.physrep.2012.02.002, arXiv:1106.0034.

[14] A. Djouadi, "The Anatomy of electro-weak symmetry breaking. II. The Higgs bosons in the minimal supersymmetric model", *Phys. Rept.* **459** (2008) 1, doi:10.1016/j.physrep.2007.10.005, arXiv:hep-ph/0503173.

[15] G. Senjanovic and R. N. Mohapatra, "Exact Left-Right Symmetry and Spontaneous Violation of Parity", *Phys. Rev. D* **12** (1975) 1502, doi:10.1103/PhysRevD.12.1502.

[16] J. F. Gunion, R. Vega, and J. Wudka, "Higgs triplets in the standard model", *Phys. Rev. D* **42** (1990) 1673, doi:10.1103/PhysRevD.42.1673.

[17] H. Georgi and M. Machacek, "Doubly charged Higgs bosons", *Nucl. Phys. B* **262** (1985) 463, doi:10.1016/0550-3213(85)90325-6.

[18] C. Degrande et al., "Accurate predictions for charged Higgs production: Closing the $m_{h^\pm} \sim m_t$ window", *Phys. Lett. B* **772** (2017) 87, doi:10.1016/j.physletb.2017.06.037, arXiv:1607.05291.

[19] ALEPH, DELPHI, L3, OPAL and LEP Collaborations, "Search for charged Higgs bosons: combined results using LEP data", *Eur. Phys. J. C* **73** (2013) 2463, doi:10.1140/epjc/s10052-013-2463-1, arXiv:1301.6065.

[20] CDF Collaboration, "Search for Higgs bosons predicted in two-Higgs-doublet models via decays to tau lepton pairs in 1.96 TeV p anti-p collisions", *Phys. Rev. Lett.* **103** (2009) 201801, doi:10.1103/PhysRevLett.103.201801, arXiv:0906.1014.

[21] D0 Collaboration, "Search for Higgs bosons of the minimal supersymmetric standard model in $p\bar{p}$ collisions at $\sqrt{s} = 1.96$ TeV", *Phys. Lett. B* **710** (2012) 569, doi:10.1016/j.physletb.2012.03.021, arXiv:1112.5431.

[22] ATLAS Collaboration, "Search for charged Higgs bosons decaying via $H^+ \to \tau\nu$ in top quark pair events using pp collision data at $\sqrt{s} = 7$ TeV with the ATLAS detector", *JHEP* **06** (2012) 039, doi:10.1007/JHEP06(2012)039, arXiv:1204.2760.

[23] CMS Collaboration, "Search for a light charged Higgs boson in top quark decays in pp collisions at $\sqrt{s} = 7$ TeV", *JHEP* **07** (2012) 143, doi:10.1007/JHEP07(2012)143, arXiv:1205.5736.

[24] ATLAS Collaboration, "Search for charged Higgs bosons through the violation of lepton universality in $t\bar{t}$ events using pp collision data at $\sqrt{s} = 7$ TeV with the ATLAS experiment", *JHEP* **03** (2013) 076, doi:10.1007/JHEP03(2013)076, arXiv:1212.3572.

[25] ATLAS Collaboration, "Search for charged Higgs bosons decaying via $H^\pm \to \tau^\pm\nu$ in fully hadronic final states using pp collision data at $\sqrt{s} = 8$ TeV with the ATLAS detector", *JHEP* **03** (2015) 088, doi:10.1007/JHEP03(2015)088, arXiv:1412.6663.

[26] CMS Collaboration, "Search for a charged Higgs boson in pp collisions at $\sqrt{s} = 8$ TeV", *JHEP* **11** (2015) 018, doi:10.1007/JHEP11(2015)018, arXiv:1508.07774.

[27] ATLAS Collaboration, "Search for charged Higgs bosons produced in association with a top quark and decaying via $H^\pm \to \tau\nu$ using pp collision data recorded at $\sqrt{s} = 13$ TeV by the ATLAS detector", *Phys. Lett. B* **759** (2016) 555, doi:10.1016/j.physletb.2016.06.017, arXiv:1603.09203.

[28] ATLAS Collaboration, "Search for charged Higgs bosons decaying via $H^\pm \to \tau^\pm\nu_\tau$ in the τ+jets and τ+lepton final states with 36 fb^{-1} of pp collision data recorded at $\sqrt{s} = 13$ TeV with the ATLAS experiment", (2018). arXiv:1807.07915. Submitted to *JHEP*.

[29] ATLAS Collaboration, "Search for charged Higgs bosons in the $H^{\pm} \to tb$ decay channel in pp collisions at $\sqrt{s} = 8$ TeV using the ATLAS detector", *JHEP* **03** (2016) 127, doi:10.1007/JHEP03(2016)127, arXiv:1512.03704.

[30] ATLAS Collaboration, "Search for a light charged Higgs boson in the decay channel $H^+ \to c\bar{s}$ in $t\bar{t}$ events using pp collisions at $\sqrt{s} = 7$ TeV with the ATLAS detector", *Eur. Phys. J.* **C73** (2013) 2465, doi:10.1140/epjc/s10052-013-2465-z, arXiv:1302.3694.

[31] CMS Collaboration, "Search for a light charged Higgs boson decaying to $c\bar{s}$ in pp collisions at $\sqrt{s} = 8$ TeV", *JHEP* **12** (2015) 178, doi:10.1007/JHEP12(2015)178, arXiv:1510.04252.

[32] CMS Collaboration, "Search for a charged Higgs boson decaying to charm and bottom quarks in proton-proton collisions at $\sqrt{s} = 8$ TeV", arXiv:1808.06575. Submitted to *JHEP*.

[33] ATLAS Collaboration, "Search for a charged Higgs boson produced in the vector-boson fusion mode with decay $H^{\pm} \to W^{\pm}Z$ using pp collisions at $\sqrt{s} = 8$ TeV with the ATLAS experiment", *Phys. Rev. Lett.* **114** (2015) 231801, doi:10.1103/PhysRevLett.114.231801, arXiv:1503.04233.

[34] CMS Collaboration, "Search for charged Higgs bosons produced via vector boson fusion and decaying into a pair of W and Z bosons using pp collisions at $\sqrt{s} = 13$ TeV", *Phys. Rev. Lett.* **119** (2017) 141802, doi:10.1103/PhysRevLett.119.141802, arXiv:1705.02942.

[35] ATLAS Collaboration, "Search for additional heavy neutral Higgs and gauge bosons in the ditau final state produced in 36 fb^{-1} of pp collisions at $\sqrt{s} = 13$ TeV with the ATLAS detector", *JHEP* **01** (2018) 055, doi:10.1007/JHEP01(2018)055, arXiv:1709.07242.

[36] CMS Collaboration, "Search for additional neutral MSSM Higgs bosons in the $\tau\tau$ final state in proton-proton collisions at $\sqrt{s} = 13$ TeV", *JHEP* **09** (2018) 007, doi:10.1007/JHEP09(2018)007, arXiv:1803.06553.

[37] CMS Collaboration, "Search for beyond the standard model Higgs bosons decaying into a $b\bar{b}$ pair in pp collisions at $\sqrt{s} = 13$ TeV", *JHEP* **08** (2018) 113, doi:10.1007/JHEP08(2018)113, arXiv:1805.12191.

[38] A. Arbey, F. Mahmoudi, O. Stal, and T. Stefaniak, "Status of the charged higgs boson in two Higgs doublet models", *Eur. Phys. J. C* **78** (2018) 182, doi:10.1140/epjc/s10052-018-5651-1, arXiv:1706.07414.

[39] M. Carena et al., "MSSM Higgs boson searches at the LHC: Benchmark scenarios after the discovery of a Higgs-like particle", *Eur. Phys. J. C* **73** (2013) 2552, doi:10.1140/epjc/s10052-013-2552-1, arXiv:1302.7033.

[40] CMS Collaboration, "The CMS trigger system", *JINST* **12** (2017) P01020, doi:10.1088/1748-0221/12/01/P01020, arXiv:1609.02366.

[41] CMS Collaboration, "The CMS experiment at the CERN LHC", *JINST* **3** (2008) S08004, doi:10.1088/1748-0221/3/08/S08004.

[42] J. Alwall et al., "The automated computation of tree-level and next-to-leading order differential cross sections, and their matching to parton shower simulations", *JHEP* **07** (2014) 079, doi:10.1007/JHEP07(2014)079, arXiv:1405.0301.

[43] P. Artoisenet, R. Frederix, O. Mattelaer, and R. Rietkerk, "Automatic spin-entangled decays of heavy resonances in Monte Carlo simulations", *JHEP* **03** (2013) 015, doi:10.1007/JHEP03(2013)015, arXiv:1212.3460.

[44] T. Sjöstrand et al., "An introduction to PYTHIA 8.2", *Comput. Phys. Commun.* **191** (2015) 159, doi:10.1016/j.cpc.2015.01.024, arXiv:1410.3012.

[45] P. Nason, "A new method for combining NLO QCD with shower Monte Carlo algorithms", *JHEP* **11** (2004) 040, doi:10.1088/1126-6708/2004/11/040, arXiv:hep-ph/0409146.

[46] S. Frixione, P. Nason, and C. Oleari, "Matching NLO QCD computations with parton shower simulations: the POWHEG method", *JHEP* **11** (2007) 070, doi:10.1088/1126-6708/2007/11/070, arXiv:0709.2092.

[47] S. Alioli, P. Nason, C. Oleari, and E. Re, "A general framework for implementing NLO calculations in shower Monte Carlo programs: the POWHEG BOX", *JHEP* **06** (2010) 043, doi:10.1007/JHEP06(2010)043, arXiv:1002.2581.

[48] T. Ježo et al., "An NLO+PS generator for $t\bar{t}$ and Wt production and decay including non-resonant and interference effects", *Eur. Phys. J. C* **76** (2016) 691, doi:10.1140/epjc/s10052-016-4538-2, arXiv:1607.04538.

[49] S. Frixione, P. Nason, and G. Ridolfi, "A positive-weight next-to-leading-order Monte Carlo for heavy flavour hadroproduction", *JHEP* **09** (2007) 126, doi:10.1088/1126-6708/2007/09/126, arXiv:0707.3088.

[50] R. Frederix and S. Frixione, "Merging meets matching in MC@NLO", *JHEP* **12** (2012) 061, doi:10.1007/JHEP12(2012)061, arXiv:1209.6215.

[51] S. Alioli, P. Nason, C. Oleari, and E. Re, "NLO single-top production matched with shower in POWHEG: s- and t-channel contributions", *JHEP* **09** (2009) 111, doi:10.1007/JHEP02(2010)011, arXiv:0907.4076. [Erratum: doi:10.1088/1126-6708/2009/09/111].

[52] E. Re, "Single-top Wt-channel production matched with parton showers using the POWHEG method", *Eur. Phys. J. C* **71** (2011) 1547, doi:10.1140/epjc/s10052-011-1547-z, arXiv:1009.2450.

[53] J. Alwall et al., "Comparative study of various algorithms for the merging of parton showers and matrix elements in hadronic collisions", *Eur. Phys. J. C* **53** (2008) 473, doi:10.1140/epjc/s10052-007-0490-5, arXiv:0706.2569.

[54] M. Czakon and A. Mitov, "Top++: A program for the calculation of the top-pair cross-section at hadron colliders", *Comput. Phys. Commun.* **185** (2014) 2930, doi:10.1016/j.cpc.2014.06.021, arXiv:1112.5675.

[55] N. Kidonakis, "Top Quark Production", in *Proceedings, Helmholtz International Summer School on Physics of Heavy Quarks and Hadrons (HQ 2013)*, p. 139. 2014. arXiv:1311.0283. doi:10.3204/DESY-PROC-2013-03/Kidonakis.

[56] P. Kant et al., "HatHor for single top-quark production: Updated predictions and uncertainty estimates for single top-quark production in hadronic collisions", *Comput. Phys. Commun.* **191** (2015) 74, doi:10.1016/j.cpc.2015.02.001, arXiv:1406.4403.

[57] K. Melnikov and F. Petriello, "Electroweak gauge boson production at hadron colliders through $o(\alpha_s^2)$", *Phys. Rev. D* **74** (2006) 114017, doi:10.1103/PhysRevD.74.114017, arXiv:hep-ph/0609070.

[58] J. M. Campbell, R. K. Ellis, and C. Williams, "Vector boson pair production at the LHC", *JHEP* **07** (2011) 018, doi:10.1007/JHEP07(2011)018, arXiv:1105.0020.

[59] NNPDF Collaboration, "Unbiased global determination of parton distributions and their uncertainties at NNLO and at LO", *Nucl. Phys. B* **855** (2012) 153, doi:10.1016/j.nuclphysb.2011.09.024, arXiv:1107.2652.

[60] CMS Collaboration, "Event generator tunes obtained from underlying event and multiparton scattering measurements", *Eur. Phys. J. C* **76** (2016) 155, doi:10.1140/epjc/s10052-016-3988-x, arXiv:1512.00815.

[61] CMS Collaboration, "Investigations of the impact of the parton shower tuning in Pythia 8 in the modelling of $\mathrm{t\bar{t}}$ at $\sqrt{s} = 8$ and 13 TeV", CMS Physics Analysis Summary CMS-PAS-TOP-16-021, 2016.

[62] GEANT4 Collaboration, "GEANT4: A simulation toolkit", *Nucl. Instrum. Meth. A* **506** (2003) 250, doi:10.1016/S0168-9002(03)01368-8.

[63] CMS Collaboration, "Particle-flow reconstruction and global event description with the CMS detector", *JINST* **12** (2017) P10003, doi:10.1088/1748-0221/12/10/P10003, arXiv:1706.04965.

[64] K. Rose, "Deterministic annealing for clustering, compression, classification, regression, and related optimization problems", *Proceedings of the IEEE* **86** (1998) 2210, doi:10.1109/5.726788.

[65] M. Cacciari, G. P. Salam, and G. Soyez, "The anti-k_{T} jet clustering algorithm", *JHEP* **04** (2008) 063, doi:10.1088/1126-6708/2008/04/063, arXiv:0802.1189.

[66] M. Cacciari, G. P. Salam, and G. Soyez, "FastJet user manual", *Eur. Phys. J. C* **72** (2012) 1896, doi:10.1140/epjc/s10052-012-1896-2, arXiv:1111.6097.

[67] CMS Collaboration, "Performance of electron reconstruction and selection with the CMS detector in proton-proton collisions at $\sqrt{s} = 8$ TeV", *JINST* **10** (2015) P06005, doi:10.1088/1748-0221/10/06/P06005, arXiv:1502.02701.

[68] A. Hoecker et al., "TMVA: Toolkit for multivariate data analysis", *PoS* **ACAT** (2007) 040, arXiv:physics/0703039.

[69] CMS Collaboration, "Performance of the CMS muon detector and muon reconstruction with proton-proton collisions at $\sqrt{s} = 13$ TeV", *JINST* **13** (2018) P06015, doi:10.1088/1748-0221/13/06/P06015, arXiv:1804.04528.

[70] CMS Collaboration, "Jet energy scale and resolution in the CMS experiment in pp collisions at 8 TeV", *JINST* **12** (2017) P02014, doi:10.1088/1748-0221/12/02/P02014, arXiv:1607.03663.

[71] CMS Collaboration, "Jet algorithms performance in 13 TeV data", CMS Physics Analysis Summary CMS-PAS-JME-16-003, 2017.

[72] CMS Collaboration, "Identification of b-quark jets with the CMS experiment", *JINST* **8** (2013) P04013, doi:10.1088/1748-0221/8/04/P04013, arXiv:1211.4462.

[73] CMS Collaboration, "Identification of heavy-flavour jets with the CMS detector in pp collisions at 13 TeV", *JINST* **13** (2018) P05011, doi:10.1088/1748-0221/13/05/P05011, arXiv:1712.07158.

[74] CMS Collaboration, "Reconstruction and identification of τ lepton decays to hadrons and ν_τ at CMS", *JINST* **11** (2016) P01019, doi:10.1088/1748-0221/11/01/P01019, arXiv:1510.07488.

[75] CMS Collaboration, "Performance of reconstruction and identification of τ leptons decaying to hadrons and ν_τ in pp collisions at $\sqrt{s} = 13$ TeV", (2018). arXiv:1809.02816. Accepted by *JINST*.

[76] CMS Collaboration, "Performance of missing transverse momentum in pp collisions at $\sqrt{s}$=13 TeV using the CMS detector", CMS Physics Analysis Summary CMS-PAS-JME-17-001, 2018.

[77] D. P. Roy, "The hadronic tau decay signature of a heavy charged Higgs boson at LHC", *Phys. Lett. B* **459** (1999) 607, doi:10.1016/S0370-2693(99)00724-8, arXiv:hep-ph/9905542.

[78] ATLAS Collaboration, "Measurement of the inelastic proton-proton cross section at $\sqrt{s} = 13$ TeV with the ATLAS detector at the LHC", *Phys. Rev. Lett.* **117** (2016) 182002, doi:10.1103/PhysRevLett.117.182002, arXiv:1606.02625.

[79] CMS Collaboration, "CMS luminosity measurements for the 2016 data taking period", CMS Physics Analysis Summary CMS-PAS-LUM-17-001, 2017.

[80] J. Butterworth et al., "PDF4LHC recommendations for LHC Run II", *J. Phys. G* **43** (2016) 023001, doi:10.1088/0954-3899/43/2/023001, arXiv:1510.03865.

[81] P. Skands, S. Carrazza, and J. Rojo, "Tuning PYTHIA 8.1: the Monash 2013 tune", *Eur. Phys. J.* **C74** (2014) 3024, doi:10.1140/epjc/s10052-014-3024-y, arXiv:1404.5630.

[82] R. J. Barlow and C. Beeston, "Fitting using finite Monte Carlo samples", *Comput. Phys. Commun.* **77** (1993) 219, doi:10.1016/0010-4655(93)90005-W.

[83] T. Junk, "Confidence level computation for combining searches with small statistics", *Nucl. Instrum. Meth. A* **434** (1999) 435, doi:10.1016/S0168-9002(99)00498-2, arXiv:hep-ex/9902006.

[84] A. L. Read, "Presentation of search results: The CL_s technique", *J. Phys. G* **28** (2002) 2693, doi:10.1088/0954-3899/28/10/313.

[85] The ATLAS Collaboration, The CMS Collaboration, The LHC Higgs Combination Group, "Procedure for the LHC Higgs boson search combination in Summer 2011", Technical Report CMS-NOTE-2011-005, ATL-PHYS-PUB-2011-11, 2011.

[86] G. Cowan, K. Cranmer, E. Gross, and O. Vitells, "Asymptotic formulae for likelihood-based tests of new physics", *Eur. Phys. J. C* **71** (2011) 1554, doi:10.1140/epjc/s10052-011-1554-0, arXiv:1007.1727. [Erratum: doi:10.1140/epjc/s10052-013-2501-z].

[87] LHC Higgs Cross Section Working Group Collaboration, "Handbook of LHC Higgs cross sections: 4. deciphering the nature of the Higgs sector", arXiv:1610.07922.

[88] M. Flechl et al., "Improved cross-section predictions for heavy charged Higgs boson production at the LHC", *Phys. Rev. D* **91** (2015) 075015, doi:10.1103/PhysRevD.91.075015, arXiv:1409.5615.

[89] C. Degrande, M. Ubiali, M. Wiesemann, and M. Zaro, "Heavy charged Higgs boson production at the LHC", *JHEP* **10** (2015) 145, doi:10.1007/JHEP10(2015)145, arXiv:1507.02549.

[90] S. Dittmaier, M. Kramer, M. Spira, and M. Walser, "Charged-Higgs-boson production at the LHC: NLO supersymmetric QCD corrections", *Phys. Rev. D* **83** (2011) 055005, doi:10.1103/PhysRevD.83.055005, arXiv:0906.2648.

[91] E. L. Berger, T. Han, J. Jiang, and T. Plehn, "Associated production of a top quark and a charged Higgs boson", *Phys. Rev. D* **71** (2005) 115012, doi:10.1103/PhysRevD.71.115012, arXiv:hep-ph/0312286.